Unraveling the Origin of Photocatalytic Deactivation in CeO 2 /Nb 2 O 5 Heterostructure Systems during Methanol Oxidation: Insight into the Role of Cerium Species

Lukasz Wolski, Oleg Lebedev, Colin Harmer, Kirill Kovnir, Hanen Abdelli, Tomasz Grzyb, Marco Daturi, Mohamad El-Roz

Unravelling the origin of photocatalytic deactivation in CeO_2/Nb_2O_5 heterostructure systems - Insight into the role of cerium species

Lukasz Wolski[a,b,*], Oleg I. Lebedev[c], Colin P. Harmer[d,e], Kirill Kovnir[d,e], Hanen Abdelli[b], Tomasz Grzyb[f], Marco Daturi[b], Mohamad El-Roz[b,*]

[a] *Faculty of Chemistry, Adam Mickiewicz University, Poznań, Uniwersytetu Poznańskiego 8, 61-614 Poznań, Poland*

[b] *Normandie Univ, ENSICAEN, UNICAEN, CNRS, Laboratoire Catalyse et Spectrochimie, 14050 Caen, France*

[c] *Laboratoire CRISMAT, ENSICAEN, CNRS UMR 6508, 14050 Caen, France*

[d] *Iowa State University, Department of Chemistry, Ames, Iowa 50011, United States of America*

[e] *U.S. Department of Energy, Ames Laboratory, Ames, Iowa, 50011, United States of America*

[f] *Department of Rare Earths, Faculty of Chemistry, Adam Mickiewicz University, Poznań, Uniwersytetu Poznańskiego 8, 61-614 Poznań, Poland*

** corresponding authors at:*
Adam Mickiewicz University, Poznań, Poland; e-mail: wolski.lukasz@amu.edu.pl (L. Wolski)
Laboratoire Catalyse et Spectrochimie, France; e-mail: mohamad.elroz@ensicaen.fr (M. El-Roz)

Key words: *niobium pentoxide; cerium dioxide; methanol photooxidation; recombination of charge carriers*

Abstract:

The study provides deep insight into the origin of photocatalytic deactivation of niobium pentoxide after doping with ceria. Of particular interest was to fully understand the role of cerium species in diminishing the photocatalytic performance of CeO_2/Nb_2O_5 heterostructures. For this purpose, ceria was loaded on niobia surfaces by wet impregnation. The as-prepared materials were characterized by powder XRD, nitrogen physisorption, UV-vis, XPS, HRTEM, and photoluminescence measurements. Photocatalytic activity of parent metal oxides (i.e. Nb_2O_5 and CeO_2) and as-prepared CeO_2/Nb_2O_5 heterostructures with different cerium loadings were tested in methanol photooxidation, a model gas-phase reaction. Deep insight into the photocatalytic process provided by *operando*-IR techniques combined with results of photoluminescence studies revealed that deactivation of CeO_2/Nb_2O_5 heterostructures resulted from increased recombination of photo-excited electrons and holes. The main factor contributing to more efficient recombination of the charge carriers in the heterostructures was the ultrafine size of the ceria species. The presence of such highly dispersed ceria species on the niobia surface provided a strong interface between these two semiconductors, enabling efficient charge transfer from Nb_2O_5 to CeO_2. However, the ceria species supported on niobia exhibited high defect site concentration which acted as highly active recombination centers for the photo-induced charge carriers.

1 Introduction

Cerium dioxide is one of the most intensively studied model heterogeneous catalysts. Hitherto, it has been established that ceria can be successfully used not only as a support for various active phases but it can also be involved as a promising active component for various reactions [1]. Recently, cerium dioxide has been thoroughly studied for applications in advanced oxidation processes, e.g. photocatalytic oxidation [2–4] or Fenton-like reactions [5–7]. Many authors have reported that doping of semiconducting metal oxides with ceria is an efficient method to improve the photocatalytic performance of parent oxides. For instance, Zhu et al. [8] have documented that CeO_2/ZnO composites displayed highly enhanced photocatalytic activity in Rhodamine B (RhB) degradation compared to pristine ZnO and CeO_2. The increase in activity of the CeO_2/ZnO heterostructures was attributed by the authors to formation of Z-scheme heterojunction, which improved the separation of photo-generated charge carriers. Improved efficiency of charge carriers separation resulting from formation of heterojunctions has also been reported for CeO_2/TiO_2 systems in photooxidation of toluene [9] and photodegradation of phenazopyridine drugs [10]. However, the above-mentioned paradigm concerning the positive role ceria doping plays in improving the photocatalytic activity of various semiconducting metal oxides has been recently rebutted by Morlando et al. [11]. The authors found that deposition of CeO_2 nanodots on the surface of TiO_2 led to significant decrease in photocatalytic activity of the as-formed composite materials. The authors claimed that the decrease in activity of CeO_2/TiO_2 nanocomposites may have resulted from scavenging of reactive oxygen species by cerium species, increased recombination of photo-excited charge carriers caused by ceria doping and/or UV shielding effects from ceria loading on the surface of TiO_2. Deactivation of photocatalysts after ceria doping was also observed for CeO_2/ZnO heterostructures [12]. According to the authors, deactivation of this catalytic system arose from the presence of ultrafine CeO_2 nanoparticles with existing surface defects which could impart some form of

reactive oxygen species scavenging property. However, no evidence supporting the above-mentioned hypotheses, explaining deactivation of TiO_2 or ZnO photocatalysts after loading of ceria species, has been provided.

Besides ZnO and TiO_2, niobium pentoxide (Nb_2O_5) is another semiconductor which has been successfully used in photocatalytic reactions [13–17]. Niobia is known for its high Brønsted acidity which can play an important role in controlling the selectivity of various processes [14,18,19]. Previous reports show the photocatalytic activity of Nb_2O_5 can also be improved by forming heterojunctions with other semiconductors (e.g. Nb_2O_5/TiO_2 [20,21], Nb_2O_5/ZnO [22], Nb_2O_5/Bi_2WO_6 [23], NiO/Nb_2O_5 [24] and Nb_2O_5/g-C_3N_4 [25]). However, to the best of our knowledge, there are no fundamental studies evaluating the influence of ceria doping on the photocatalytic activity of niobium pentoxide. In view of the recent results, reporting the ambiguous negative/positive role of ceria dopant in CeO_2/ZnO and CeO_2/TiO_2 heterostructures, a fundamental evaluation of the cerium species' role in controlling the activity of niobia-based photocatalysts is crucial for rational development of ceria-containing photocatalysts.

The present study establishes the influence of ceria doping on the structure, texture, and photocatalytic performance of niobium pentoxide. Ceria species were loaded on niobia surface by wet impregnation. Photocatalytic activity of parent metal oxides (i.e. Nb_2O_5 and CeO_2) and as-prepared CeO_2/Nb_2O_5 heterostructures with different ceria loading was tested in methanol oxidation, a well-known model reaction which allows to determine relationship between properties of materials and their catalytic performance. *Operando*-IR techniques provided insight into the mechanism of the photocatalytic process across CeO_2/Nb_2O_5 heterostructures while elucidating the role individual components of each heterostructure play in methanol photooxidation [26–28].

2 Experimental

2.1 Synthesis of Nb_2O_5

Niobium pentoxide was synthesized using the hydrothermal procedure described by Murayama et al. [29]. In a typical synthesis route, ammonium niobate(V) oxalate hydrate (Sigma-Aldrich, $C_4H_4NNbO_9$ x H_2O, 99.99%) (9.0894 g, 30 mmol) was dissolved in 200 mL of deionized water. Following 1 h of vigorous stirring, the pellucid solution was sealed in a teflon-lined stainless-steel autoclave and heated for 24 h at 175 °C. The solid formed during hydrothermal treatment was then separated by filtration, washed with deionized water, dried at room temperature and calcined for 2 h at 400 °C (temperature ramp: 1.6 °C/min). The as-prepared material was denoted as Nb_2O_5.

2.2 Loading of ceria species on the niobia support

Ceria species were loaded on the surface of Nb_2O_5 via a facile wet impregnation method. In a typical synthesis, 6 g of as-prepared Nb_2O_5 was dispersed in 10 mL of deionized water. Meanwhile, cerium(III) nitrate hexahydrate (Sigma-Aldrich, 99.99%) was dissolved in 35 mL of deionized water (the amount of cerium source was adjusted to obtain 1.0, 5.0 or 10.0 wt.% of Ce on the niobia support). Next, the solution of cerium(III) nitrate hexahydrate was stirred into the mixture containing niobium pentoxide dispersed in water. Following 1 h of agitation at room temperature, the mixture was transferred to a round bottom flask and sonicated for 10 min. In the next step, water was evaporated from the mixture using a rotary evaporator and the as-obtained powder was dried in a furnace at 80 °C for 12 h. Finally, the dry powder was calcined at 400 °C for 2 h (temperature ramp: 1.6 °C/min). The as-prepared ceria-doped catalysts containing 1.0, 5.0 or 10.0 wt.% of Ce were labelled as $Ce1/Nb_2O_5$, $Ce5/Nb_2O_5$, and $Ce10/Nb_2O_5$, respectively.

Mechanical CeO_2/Nb_2O_5 mixtures were prepared using Nb_2O_5 and commercial CeO_2. For this purpose, appropriate amounts of metal oxides were mixed with small amount of

deionized water and then crushed in agate mortar to get homogeneous mixture. Next, the as-obtained mechanical mixtures of metal oxides were dried overnight at 70 °C to obtain dry powders. The as-prepared materials were used as reference samples.

2.3 Characterization of catalysts

The catalysts were characterized with the use of inductively coupled plasma-optical emission spectrometry (ICP-OES), nitrogen physisorption, powder X-ray diffraction (PXRD), high resolution transmission electron microscopy (HR TEM), UV-visible spectroscopy (UV-vis), X-ray photoelectron spectroscopy (XPS), and photoluminescence measurements (PL).

Powder X-ray diffraction patterns were collected on a benchtop Rigaku Miniflex 600 with Cu K_α radiation (λ= 1.5406 Å) and Ni-K_β filter. Peak locations of each sample were refined against a Si internal standard (Si 640d, *Fd*-3*m*, *a* = 5.43123 Å) via Rietveld refinement in GSAS-II [30]. Rietveld refinement was initiated by determining sample displacement from the Si internal standard. Then size and preferred orientation were refined to best fit each sample before refining unit cell parameters.

Transmission electron microscopy (TEM) was performed using JEM ARM200F cold FEG probe and image aberration corrected microscope, operated at 200 kV and equipped with large angle CENTURIO EDX detector, Orius Gatan CCD camera and Quantum GIF. The TEM samples were prepared in conventional way – depositing solution of the material in ethanol on a carbon holey Cu grid.

Diffuse reflectance UV–vis spectra (DR UV–vis) were recorded on a Varian Cary 300 Scan spectrophotometer equipped with a diffuse reflectance accessory. Spectra were recorded at room temperature from 200 to 800 nm using Spectralon as a reference material.

Photoluminescence properties were studied at room temperature using a PIXIS:256E Digital CCD Camera equipped with an SP-2156 Imaging Spectrograph (Princeton Instruments)

and Opolette 355LD UVDM tuneable laser as the excitation source (with repetition rate 20 Hz; 0.5 mJ pulse energy at 250 nm). All spectra were corrected for spectral response of the equipment. The beam size and laser powers were determined by a 10A-PPS power meter (Ophir Photonics).

The N_2 adsorption-desorption isotherms were obtained at −196 °C using a Micromeritics ASAP 2020 Physisorption Analyzer. Before the measurements, samples were degassed at 120 °C for 10 h. The surface area of the materials obtained was estimated by the Brunauer–Emmett–Teller (BET) method.

X-ray photoelectron spectroscopy (XPS) was performed using an ultra-high vacuum photoelectron spectrometer based on Phoibos150 NAP analyzer (Specs, Germany). The analysis chamber was operated under vacuum with a pressure close to 5×10^{-9} mbar and the sample was irradiated with a monochromatic Al Kα (1486.6 eV) radiation. Any charging that occurred during the measurements (due to incomplete neutralization of ejected surface electrons) was accounted for by rigidly shifting the entire spectrum by a distance needed to set the binding energy of the C1s assigned to adventitious carbon to the assumed value of 284.8 eV.

2.4 Photocatalytic tests

The photocatalysts were pressed into self-supported wafers (Ø =16 mm, m ≈ 11.7 mg/cm^2) of about 65 ± 2 μm in thickness. The outlet gas phase evolution was followed by both IR spectroscopy and mass spectrometry. FT-IR spectra of the outlet gas phase and of the samples were collected with a Nicolet 5700 FT-IR spectrometer (64 scans/spectrum) equipped with an MCT detector. The *operando-IR* system was connected to a flow set-up [31]. Gases were introduced into the lines by mass flow controllers. The system allows the two gas mixtures, the so-called "activation" and "reaction" flows, to be prepared and sent independently to the reactor cell. The "Sandwich" type reactor-cell used in this study is described in reference [32]. It was made of a stainless-steel cylinder that carries a toroidal sample holder in its center, where the

catalyst self-supporting wafer was placed. Tightness was obtained by O-rings, and the dead volume (typically defined as the residual space between each sample face and the windows) was reduced to about 0.4 mL by filling the empty space with KBr windows placed on each side of the sample holder. The sample analysis was made possible without the superposition of the gas phase signal and fluid dynamics. Gases were introduced to the sample and evacuated by two 1/8-inch OD pipes connected to the opposite sides of the sample holder. In this study, UV irradiation was carried using a UV light guide (A10014-50-0110) mounted at the entrance to the IR cell and connected to a polychromatic light of Xe-Hg lamp (LC8 spot light Hamamatsu, L10852, 200 W) equipped with a filter to enable monochromatic UV irradiation (λ = 365 nm). More details on the *operando-IR* system for photocatalysis can be found in references [32] and [33]. The employed configuration allowed a low partial pressure of methanol to be achieved using a saturator at controlled temperature. The gas mixture composition was fixed then at 0.12 vol. % methanol and 20 vol. % O_2 in Ar and the total flow was adjusted to 20 cm^3/min. Outlet gasses were characterized by a Pfeiffer Omnistar mass spectrometer. FT-IR spectra of the gas phase were collected using a gas microcell. The conversions were calculated at the steady state.

3 Results and discussion

3.1 Photocatalytic tests

Photocatalytic activity of materials was tested via methanol oxidation in gas phase. The results are shown in **Fig. 1a**. The highest methanol conversion of 24.6 % was observed for undoped Nb_2O_5. Commercial CeO_2 was significantly less active than undoped niobium pentoxide and its activity at 5.3 %. As can be seen from **Fig. 1a**, all ceria-doped samples exhibited significantly lower activity than unmodified Nb_2O_5. In the case of Ce1/Nb_2O_5 activity was reduced by more than 50 % compared to pristine niobia (24.6 % vs. 11.9 % of methanol conversion for Nb_2O_5 and Ce1/Nb_2O_5, respectively). More pronounced decrease in the activity of the composite catalysts was observed for Ce5/Nb_2O_5. Interestingly, for Ce10/Nb_2O_5

photocatalytic activity of the heterostructure was totally quenched. There were no products formed during the methanol photooxidation over this catalyst.

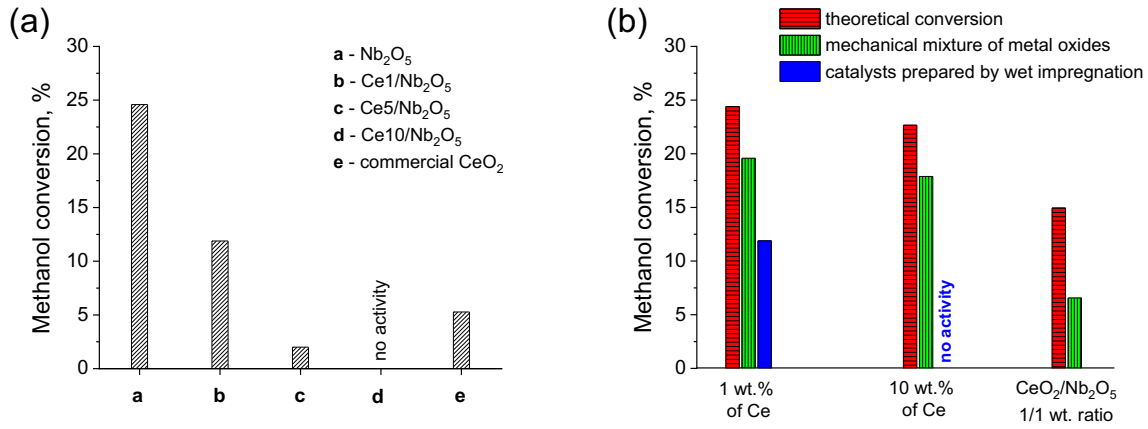

Fig. 1. (a) activity of catalysts in methanol photooxidation at the steady state for 2 h of reaction; **(b)** graph presenting differences between activity of ceria-doped catalysts prepared by wet impregnation, mechanical mixtures of metal oxides and theoretical methanol conversion expected at the given concentration of Nb_2O_5 and CeO_2 in the composite materials (theoretical conversion of methanol was estimated by summing up activity of given amounts of commercial CeO_2 and undoped Nb_2O_5 in the heterostructures). Mechanical mixture of metal oxides was prepared using undoped Nb_2O_5 and commercial CeO_2 (see experimental section).

To gain deeper insight into the quenching of catalysts' activity after loading of ceria on niobia we performed additional measurements with mechanical mixtures of metal oxides as reference samples. We found that activity of these mechanical mixtures of metal oxides containing 1 wt.% and 10 wt.% of Ce was only slightly lower than that observed for unmodified Nb_2O_5 (see **Fig. 1b**). Interestingly, the activity of mechanical mixtures of CeO_2 and Nb_2O_5 oxides was not quenched even at very high concentration of CeO_2 in the composite material (Nb_2O_5:CeO_2 weight ratio of 1:1). As can be seen from **Fig. 1**, such mixture of metal oxides was still slightly more active than commercial CeO_2. To shed light on the role of cerium species in deactivation of ceria-doped samples, prepared by wet impregnation, we compared the activity

of these materials with the activity of mechanical mixtures of metal oxides and theoretical activity of the composite materials expected at given concentration of CeO_2 and Nb_2O_5 in the heterostructures (theoretical methanol conversion was estimated by summing up the activity of given amount of Nb_2O_5 and commercial CeO_2 in the composite). According to our results, the activity of mechanical mixtures of metal oxides was always lower than the expected theoretical values, but was still significantly higher than the activity of samples prepared by wet impregnation (see **Fig. 1b**). This observation led us to conclude that deactivation of the composite catalysts prepared by wet impregnation should be somehow related to the unique properties of these materials and their interaction.

To further probe the role of the ceria dopant in the photocatalytic process, *operando*-IR studies have been performed. According to literature [34], the first step of methanol photooxidation is the adsorption of methyl alcohol on the catalyst surface and consequently the formation of surface methoxy species. *Operando*-IR studies show that exposure of all catalysts to the gas feed led to immediate disappearance of IR bands typical of surface hydroxyl groups of niobia and ceria (e.g. IR bands at ca. 3662 cm^{-1} characteristic of bridged OH groups in the fluorite structure of ceria [35,36]) and appearance of several new IR bands typical of adsorbed methanol molecules (e.g. IR bands in the range from 2750 cm^{-1} to 3000 cm^{-1} [33,37]; see **Fig. S1**, *Supporting Information*). Detailed analysis of the adsorbed methoxy species, in the range of wavelengths shown in **Fig. S1**, is problematic since the typical C-H vibration bands overlap with the characteristic O-H vibration bands of adsorbed water. Thus, detailed analysis of adsorbed species on catalysts surfaces was performed on the basis of FTIR spectra in the range of wavenumbers where characteristic vibrations of adsorbed methoxy groups are not overlapped with other vibrational bands (i.e. at 1200-1000 cm^{-1} [38]). **Fig. 2** shows surface FTIR spectra of catalysts at the equilibrium state during methanol adsorption under dark conditions. In the case of ceria is easy to identify the bands due to linearly (1112 cm^{-1}) and two-fold (1057

cm^{-1}) coordinated methoxys on Ce^{4+} [38]. The components at 1039 cm^{-1} is assigned to bridged species on Ce^{4+} cations in the proximity of an oxygen vacancy [38]. The other bands observed at higher wavenumbers are due to carbonate impurities belonging to ceria exposure to air [38] and to residual oxalates on the surface of niobia. Analysis of IR spectra recorded for niobia-based samples allowed discrimination of three components at ca. 1158, 1125 and 1105 cm^{-1}. The first component at ca. 1158 cm^{-1} is characteristic of $\rho(CH_3)$ rocking mode of methoxy species [39], while the latter two IR bands are typical of ν(OC) vibration modes of linearly (1125 cm^{-1}) and may be two-fold (or another linear species coordinated on different exposed crystal planes – at 1105 cm^{-1}) coordinated methoxy species on niobia [40]. We found no significant differences in the forms and concentration of methoxy species on the surface of unmodified Nb_2O_5 and ceria-doped samples prepared by wet impregnation. Even at relatively high loading of cerium species (10 wt.%), no noticeable IR bands typical of aforementioned methoxy species bonded to ceria surface were found. In view of these observations, we concluded that quenching of niobia activity through loading of ceria by wet impregnation cannot be attributed to covering of niobia surface by cerium species and/or hindering of niobia ability to adsorb methanol molecules.

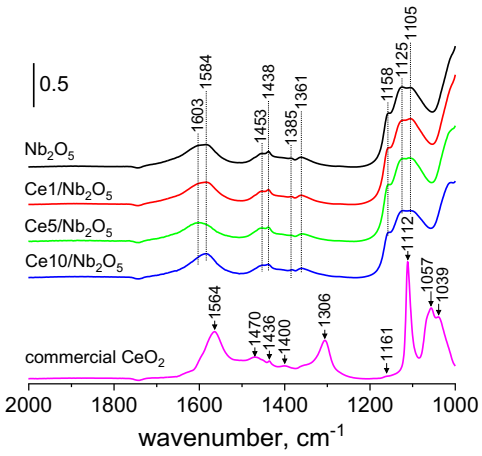

Fig. 2. FTIR spectra of catalysts surfaces at steady state during methanol adsorption under dark conditions.

The second step in photocatalytic oxidation of methanol is oxidation of adsorbed methoxy species to formaldehyde [34]. The as-formed formaldehyde can then be desorbed from catalyst surface or further transformed into other products such as methyl formate, formic acid, or carbon dioxide. According to literature, oxidation of formaldehyde to other products leads to appearance of some reaction intermediates, such as adsorbed formate species, characterized by the vibrational bands at ca. 1565, 1371 and 1356 cm^{-1} for commercial CeO_2 and ca. 1577, 1385 and 1365 cm^{-1} for niobia-based photocatalysts [32,34]. As can be seen from sample FTIR spectra of undoped Nb_2O_5 and commercial CeO_2 shown in **Fig. 3a**, typical IR bands for these reaction intermediates showed up immediately after irradiation of the catalysts with UV light and continue to increase intensity upon irradiation. The increase in intensity of typical IR bands of adsorbed formate species was associated with a decrease in intensity of characteristic IR bands of adsorbed methanol molecules (IR bands in the range 1200-1000 cm^{-1}). This observation led us to conclude that methanol is efficiently oxidized on the surface of these two unmodified metal oxides. Even, on ceria the oxidation proceeds until CO_2, as witnessed by the formation of bidentate carbonates on the surface of the samples (bands at 1594 and 1304 cm^{-1}) [38]. However, a different trend was observed for ceria-doped samples prepared by wet impregnation. As can be seen from **Fig. 3b**, the changes in intensity of IR bands characteristic of adsorbed formate species was significantly suppressed for the $Ce1/Nb_2O_5$ and $Ce5/Nb_2O_5$ catalysts. In the case of reaction with the use of $Ce10/Nb_2O_5$, almost no changes in intensity of IR bands typical of adsorbed formate species were found. Also, no changes were observed for this catalyst in the range of wavenumbers characteristic of adsorbed methoxy species (see **Fig. 3a**). It is worth noting that for all niobia-based samples methanol conversion was found to be proportional to the intensity of IR bands characteristic of adsorbed formate species (see **Fig. 3c**). Thus, IR experimental data indicated that a decrease in activity of heterostructures

prepared by wet impregnation resulted from their reduced ability to oxidize methanol molecules adsorbed on niobia surface.

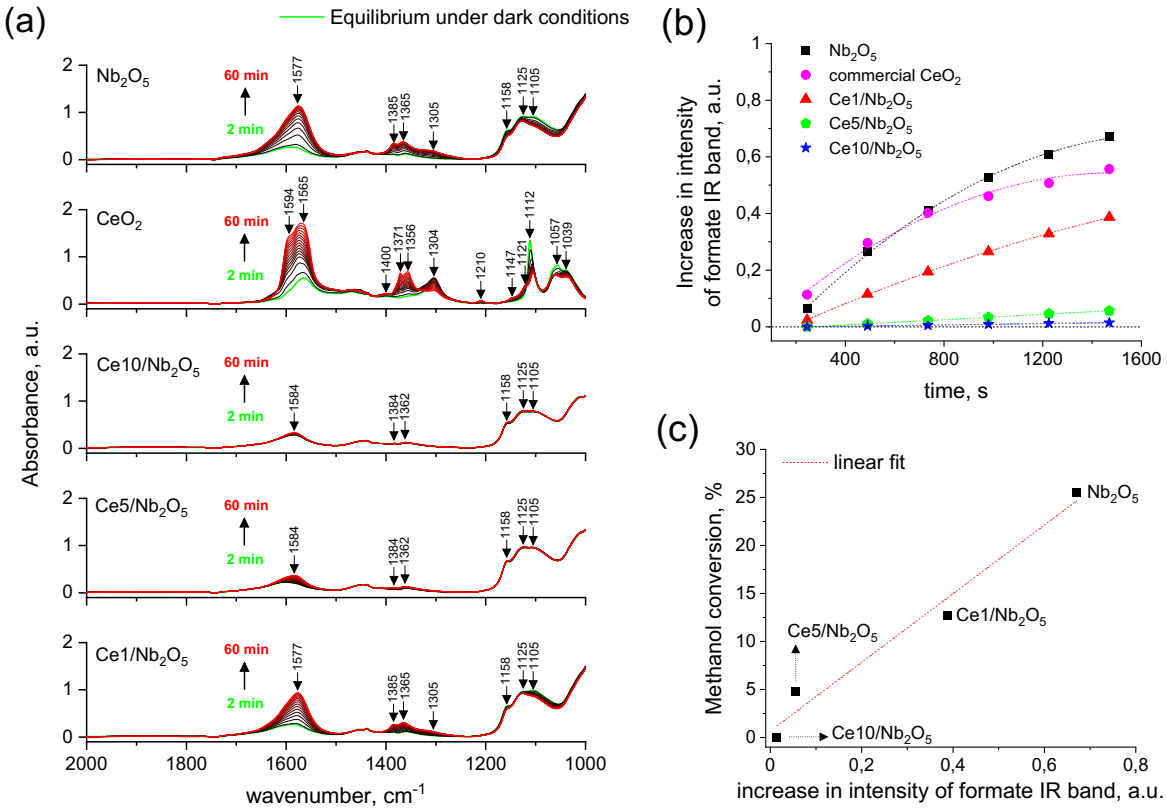

Fig. 3 (a) FTIR spectra of catalysts surfaces recorded at the beginning of photocatalytic oxidation of methanol under UV light (λ = 365 nm); **(b)** graph presenting changes in intensity of the most intense IR band typical for adsorbed formate species (i.e. band at 1577 cm^{-1} for Nb_2O_5 and $Ce1/Nb_2O_5$; band at 1584 cm^{-1} for $Ce5/Nb_2O_5$ and $Ce10/Nb_2O_5$; and band at 1565 cm^{-1} for commercial CeO_2) at the beginning of photocatalytic process; **(c)** relationship between activity of catalysts and increase in intensity of the most intense IR band typical of adsorbed formate species (increase in the intensity of the IR band was calculated by subtracting the intensity of the IR band at equilibrium state during methanol adsorption under dark conditions from the intensity of the IR band after about 24 minutes of photocatalytic reaction).

3.2 Characterization of catalysts

To understand the origin of photocatalytic deactivation of ceria-doped samples prepared by wet impregnation, the as-prepared catalysts were precisely characterized by a variety of complementary methods, providing information about their composition, structure, texture, optical and electronic properties.

To confirm presence of cerium species on the niobia surface, chemical composition of catalysts was analyzed with the use of ICP-OES. As can be seen from **Table 1**, for all ceria-containing catalysts, real loading of Ce was only slightly lower than the assumed values and was found to be of 0.7, 3.7 and 7.9 wt.% of Ce for Ce1/Nb_2O_5, Ce5/Nb_2O_5 and Ce10/Nb_2O_5, respectively.

Table 1. Characteristics of niobia-based catalysts.

Catalyst	BET surface area [m^2/g]	Average pore size[a], [nm]	Ce loading[b] [wt.%]
Nb_2O_5	157	8.8	-
Ce1/Nb_2O_5	153	9.0	0.7
Ce5/Nb_2O_5	156	8.3	3.7
Ce10/Nb_2O_5	143	8.1	7.9
CeO_2[c]	-	-	-

[a] estimated with the use of BJH method from adsorption branch; [b] determined with the use of ICP-OES; [c] commercial CeO_2

Structure of materials was characterized by powder X-ray diffraction (λ = 1.5406 Å). As can be seen from **Fig. 4**, PXRD patterns of all samples exhibited two distinct diffraction peaks at 22.7 and 46.3 ° 2θ, which are similar to the reported PXRD pattern of deformed orthorhombic Nb_2O_5 phase [29]. It should be noted that no crystalline CeO_2 or other cerium species was identified for all ceria-doped materials, indicating that ceria species existed in amorphous form or were highly dispersed on niobia surface.

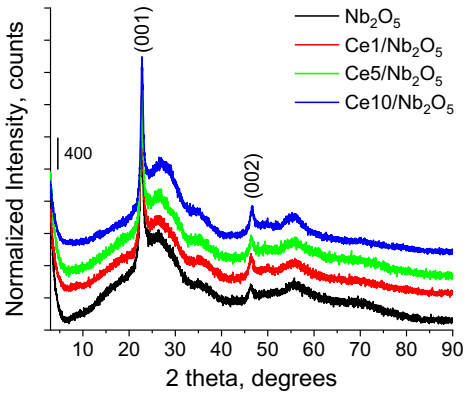

Fig. 4. PXRD patterns of catalysts normalized to the intensity of (001) peak.

Detailed analysis of electron diffraction (ED) patterns and high resolution TEM images of niobium pentoxide led us to observe discrepancy between the previously reported deformed orthorhombic structure of Nb_2O_5 [29] and the structure obtained in this study. For this reason, identification of a niobia structural model was determined by first attempting to fit the PXRD data to known structures. Although we did not find any matches to known structurally characterized Nb-O binaries, a search among tantalum oxides (note similar size of Ta and Nb) revealed orthorhombic Ta_2O_5 crystallizing in the *Cmmm* space group as a reasonable fit [41]. Ta_2O_5 is composed of Ta-O octahedra with Ta on the *ab*-plane bridged by equatorial O atoms and stacked along the *c*-axis by axially bridging O atoms. In this model the equatorial O atoms are fully occupied with half occupancy for the axial O site. This is an average structure which was shown to be incommensurately modulated. The equivalent atomic size and bonding characteristics between Nb and Ta allowed us to build an isostructural Nb_2O_5 model **(Fig. S2**, *Supporting Information*). A further database search verified no previously reported Nb-O binaries in the orthorhombic *Cmmm* space group.

Analysis of PXRD data collected with Si internal standard demonstrates that loading of ceria on niobia by wet impregnation resulted in a slight shift of the diffraction peaks at 22.7 and 46.3 °2θ towards higher angles (see **Fig. S3**, *Supporting Information*). Rietveld refinement of

our Nb_2O_5 model against PXRD data from each sample collected with a Si internal standard revealed a slight compression of the *c*-parameter of the niobia structure with increasing Ce loading (see **Table 2**). The highest decrease in the *c*-parameter value was typical of the sample with the highest concentration of ceria dopant, i.e. $Ce10/Nb_2O_5$. In view of these observations, we claim that cerium species loaded on Nb_2O_5 by wet impregnation strongly interacted with the niobia support.

Table 2. Calculated unit cell parameter c obtained from Rietveld refinement of PXRD data with Si internal standard.

Catalyst	c-parameter, [Å]	Rwp, [%]	GoF
Nb_2O_5	3.9147(4)	2.84	1.22
$Ce1/Nb_2O_5$	3.9146(3)	2.88	1.24
$Ce5/Nb_2O_5$	3.9076(3)	3.2	1.39
$Ce10/Nb_2O_5$	3.9009(4)	3.56	1.66

To confirm the novel orthorhombic *Cmmm* structure of Nb_2O_5 proposed by PXRD, electron diffraction (ED), high-angle annular dark field scanning TEM (HAADF-STEM) imaging and annular bright field STEM (ABF-STEM) analyses were performed. The chemical composition and Ce distribution over the samples was confirmed by STEM-EDX elemental mapping. It was found that irrespectively of Ce amount, ceria-doped samples showed similar features as for undoped Nb_2O_5 (see **Figs. 5** and **S4**, respectively). All samples consisted of needle-type nanostructures with typical dimensions: length around 20-40 nm and diameter 7-10 nm. They were stuck together in a random array, creating nanopores in the volume of the sample. Corresponding ring ED pattern of ceria-doped niobium pentoxide (**Fig. 5d** insert) can

be fully indexed based on proposed orthorhombic *Cmmm* structure. No extra rings belonging to Ce or Ce-O structures are present in agreement with PXRD data. EDX elemental mapping in STEM mode evidenced homogeneous distribution of cerium species over Nb_2O_5 sample (**Fig. 5b**). STEM–EDX and ED studies support conclusion drawn based on PXRD studies regarding amorphous character or very high dispersion of cerium species on niobia surface.

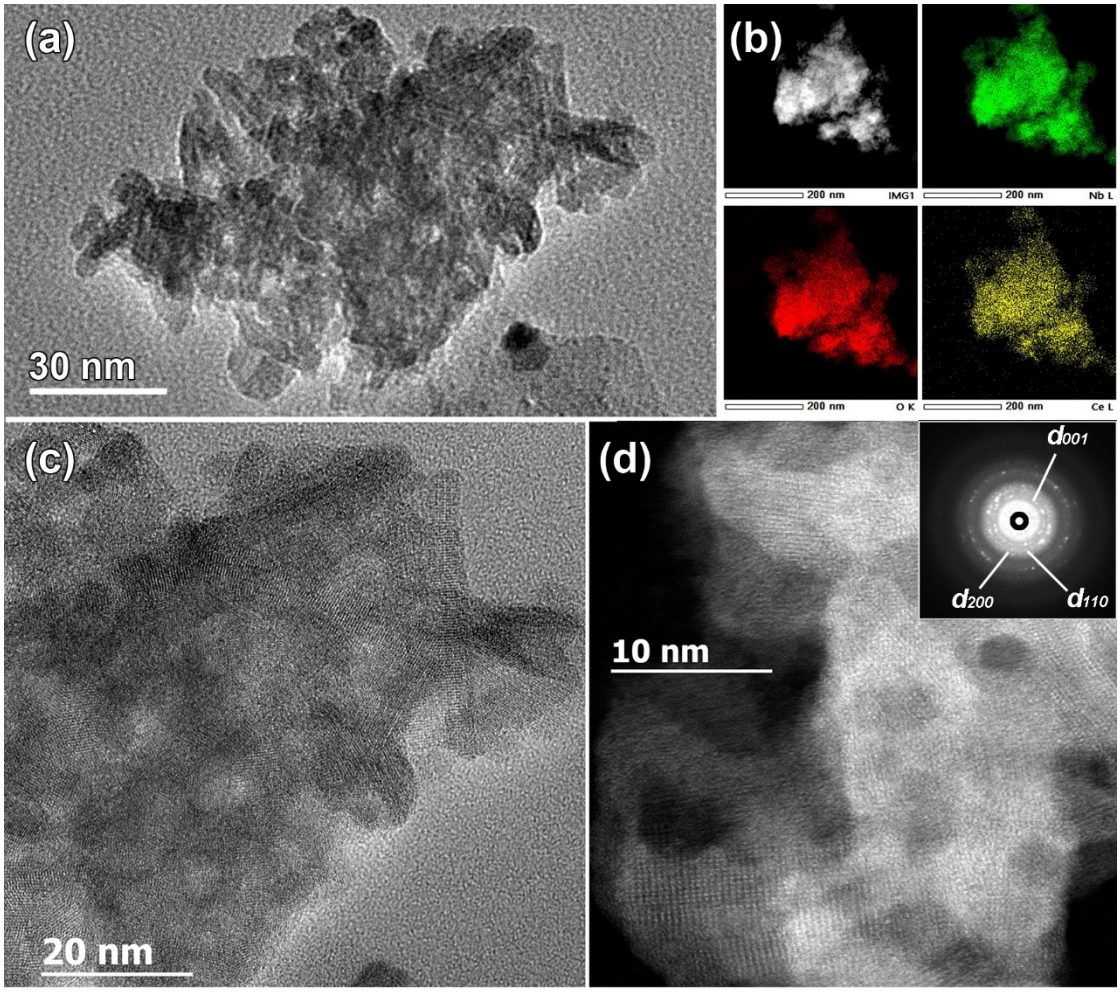

Fig.5 (a) bright field low magnification TEM image of representative ceria-doped sample prepared by wet impregnation; **(b)** low magnification HAADF-STEM image and simultaneously acquired EDX elemental mapping of Nb L, Ce L and O K; **(c)** HRTEM and **(d)** HAADF-STEM images of representative Ce/Nb_2O_5 sample.

High-resolution HAADF-STEM and simultaneously acquired ABF-STEM images along the main crystallographic zones, [010] and [110], agree with the structural model

determined by PXRD (see insert in **Fig. 6**). Using two complementary techniques, such as high resolution HAADF-STEM and ABF-STEM, provides information about position of heavy (Nb, Ce) and light (O) elements. Regardless of imperfect orientation of nanostructures due to small size exactly along zone axis, the overlaid structural model shows good correspondence to the experimental images. Due to the relatively large difference in atomic numbers between Nb(41) and Ce(58), it should be possible to distinguish positions of these two atoms in high resolution HAADF-STEM images. However, no difference in atomic columns contrast in HAADF-STEM images was detected, suggesting very high dispersion of cerium species on the niobia surface.

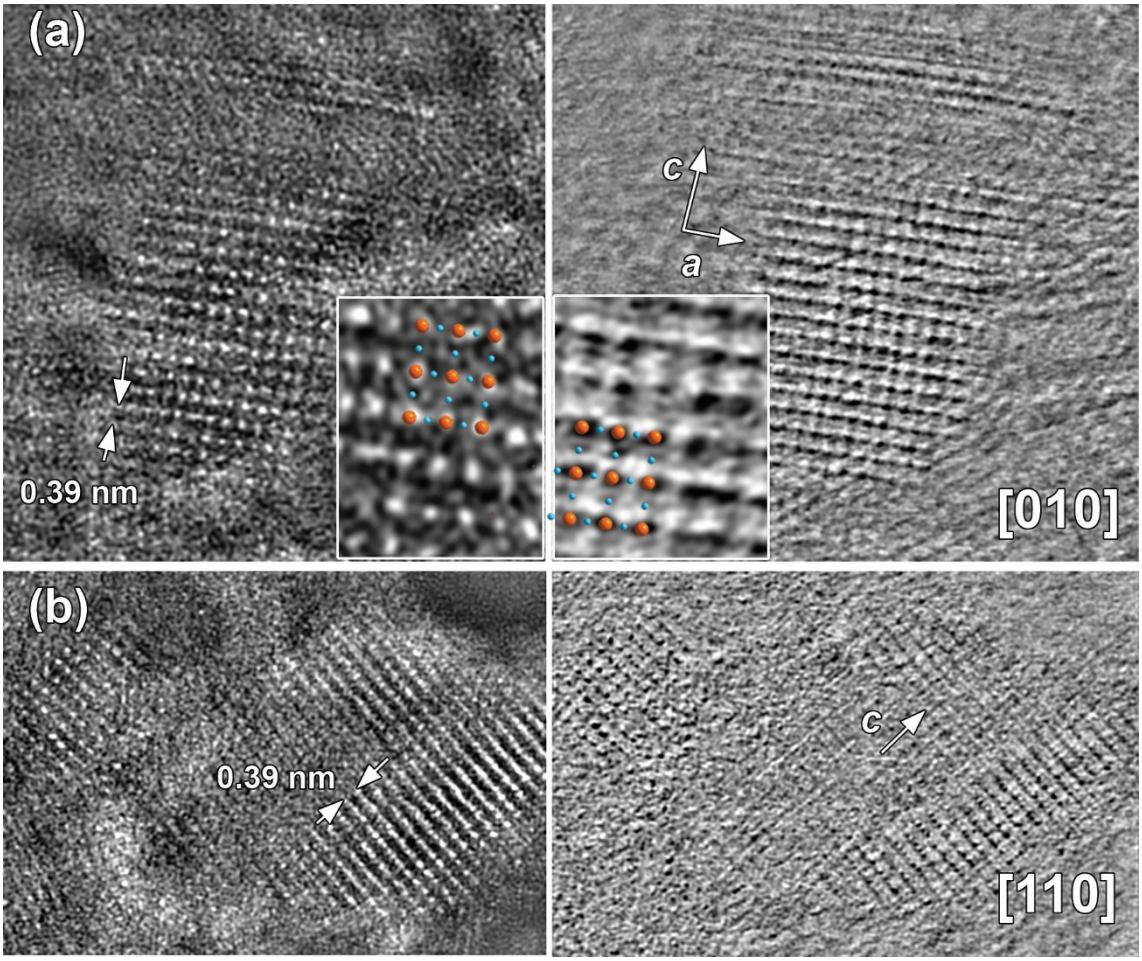

Fig.6 HAADF –STEM and simultaneously acquired ABF-STEM high resolution images along two main crystallographic zone axis **(a)** [010] and **(b)** [110] of orthorhombic *Cmmm* Nb_2O_5

structure. The magnified [010] HAADF-STEM and ABF-STEM images together with overlaid structural model are given as insert.

Texture of the catalysts was characterized with the use of low-temperature nitrogen adsorption-desorption measurements. As can be seen from **Fig. 7a**, all isotherms were of type IV(a) indicating mesoporous structure of the catalysts [42]. Textural parameters of materials estimated from nitrogen physisorption are summarized in **Table 1**. The highest BET surface area of 157 m^2/g was observed for undoped niobium pentoxide. Deposition of cerium species on niobia by wet impregnation led to decrease in the catalysts surface area, but differences between samples were insufficient to justify drastic difference in catalytic activities. The lowest surface area of 143 m^2/g was characteristic of the catalyst containing the highest amount of ceria dopant, i.e. $Ce10/Nb_2O_5$. **Fig. 7b** shows that loading of ceria on niobia support also had negligible influence on textural properties of the Nb_2O_5-based samples. All the catalysts exhibited broad pore size distribution ranging from ca. 2 nm to more than 50 nm. Average pore size estimated for all the catalysts from adsorption branch using Barrett-Joyner-Halenda (BJH) method ranged from 8 to 9 nm (see **Table 1**). The negligible influence of ceria dopant on BET surface area and pore size distribution estimated for the catalysts is further evidence of the high dispersion of cerium species on niobia surface, which is also coherent with the presence of cerium hydroxyls in the IR spectra reported above.

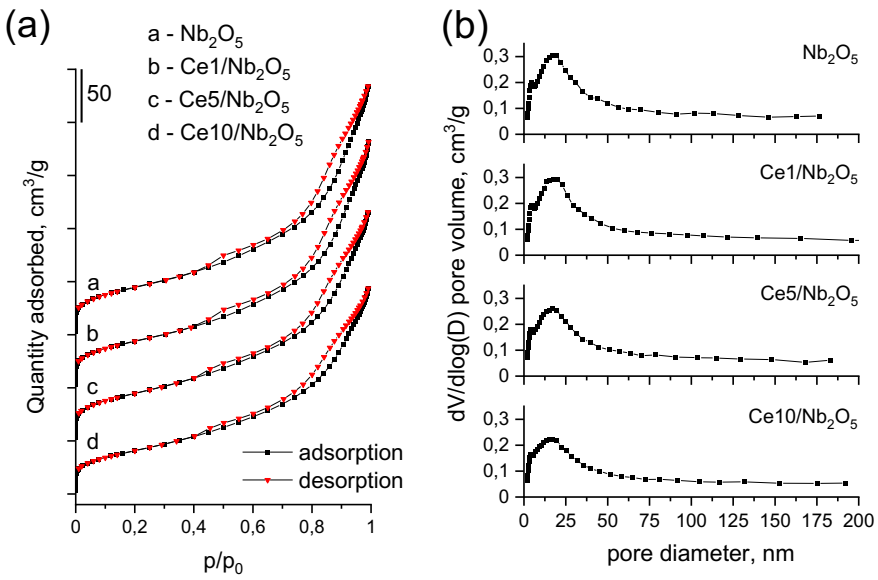

Fig. 7. (a) Low-temperature nitrogen adsorption-desorption isotherms of catalysts; **(b)** pore size distribution estimated for the catalysts from adsorption branch of N_2 isotherms using BJH method.

Optical properties of each catalyst was studied by diffuse-reflectance UV-vis spectroscopy. As can be seen from **Fig. 8a**, undoped niobia exhibited a broad absorption band with maximum absorbance at ca. 272 nm. According to literature [43], this absorption band is typical of charge transfer transitions from O^{2-} to Nb^{5+} which are associated to the energy gap between the O 2p valence band and the Nb 4d conduction band of Nb_2O_5 bulk. Commercial CeO_2 exhibited two absorption bands with maximum intensities centred at ca. 352 and 268 nm. According to literature [44,45], these absorption bands are attributed to $O^{2-} \rightarrow Ce^{4+}$ charge transfer transitions and inter-band transitions, respectively. As can be seen from **Fig. 8a**, deposition of cerium species on niobia increased ability of the composite materials to absorb light in the range of wavelengths typical of $O^{2-} \rightarrow Ce^{4+}$ charge transfer transitions. It is worth noting that the increase in light absorption observed for ceria-doped samples was proportional to the amount of cerium. The higher concentration of cerium species in the composite material, the higher the

materials ability to absorb light in the range of wavelengths typical of $O^{2-} \rightarrow Ce^{4+}$ charge transfer transitions.

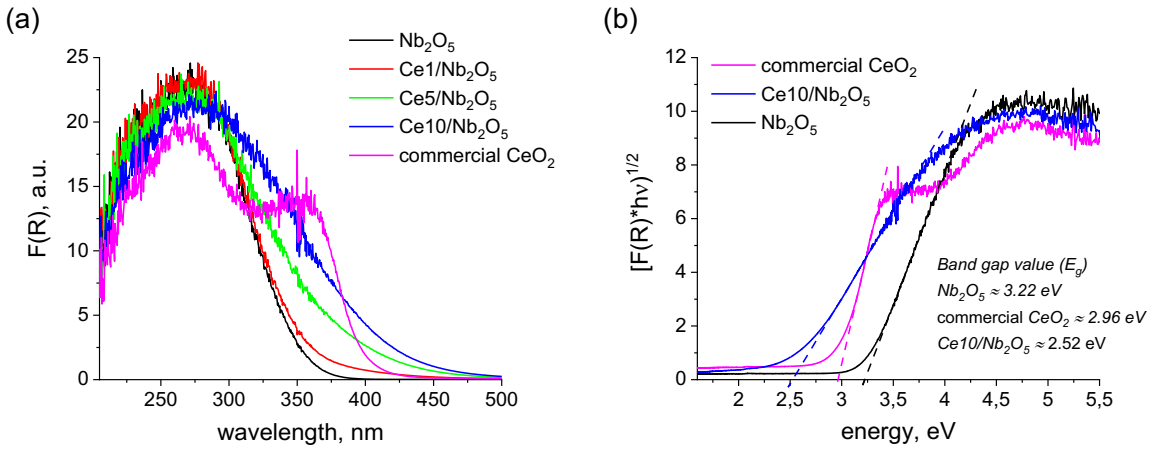

Fig. 8. (a) Diffuse-reflectance UV-vis spectra of catalysts; **(b)** results of band gap estimation using Tauc plot method for selected catalysts.

Band gap values estimated for undoped Nb_2O_5 and commercial CeO_2 using Tauc's plot method were of 3.22 and 2.96 eV, respectively, and are in agreement with previous literature data concerning optical properties of Nb_2O_5 [16,20,46] and CeO_2 [47,48]. Interestingly, composite material prepared by loading 10 wt.% of Ce on niobia by wet impregnation exhibited significantly lower band gap value than that observed for both pristine metal oxides (see **Fig. 8b**). Such decrease in band gap value of the composite material may result from formation of large quantity of defect sites in the structure of CeO_2 (e.g. Ce^{4+} ions with neighboring oxygen defects) which shifted the absorption edge of ceria towards higher wavelengths (i.e. lower energy values) [49].

To get a deeper insight into oxidation state of metals in the composite materials, the catalysts were characterized by X-ray photoelectron spectroscopy (**Fig. 9**). Nb 3d region of unmodified Nb_2O_5 was characterized by two components, namely Nb $3d_{5/2}$ and Nb $3d_{3/2}$, with the binding energy of 207.3 eV and 210.0 eV, respectively. According to literature [50], these components are assigned to Nb^{5+} species in bulk Nb_2O_5. In the case of ceria-doped samples

prepared by wet impregnation Nb 3d peaks overlapped with the peak typical of Ce $4p_{3/2}$. Precise deconvolution of experimental data led us to distinguish these components (see **Fig. 9**). The only form of niobium species in all heterostructures was Nb^{5+}. Deconvolution of Ce 3d spectra of commercial CeO_2 allowed distinguishing ten components, namely v_0, v, v', v'', v''', u_0, u, u', u'', u''' (see Fig. 9). According to literature [51–53], v, v'', v''' and u, u'', u''' are assigned to Ce^{4+} species, while v_0, v' and u_0 and u' are attributed to Ce^{3+} species. Analysis of Ce 3d XP spectra of ceria-doped samples prepared by wet impregnation was more complex due to low intensity of peaks at low cerium loadings. To avoid misinterpretation of experimental data we have omitted deconvolution of Ce 3d spectra collected for $Ce1/Nb_2O_5$ and $Ce5/Nb_2O_5$. Nevertheless, it is important to stress that Ce 3d spectra recorded for these two samples had different shape than that observed for commercial CeO_2. The most important difference can be considered in terms of a very low relative contribution of components characteristic of Ce^{4+} species, in particular u''' which is not overlapped with other peaks (see **Fig. 9**).

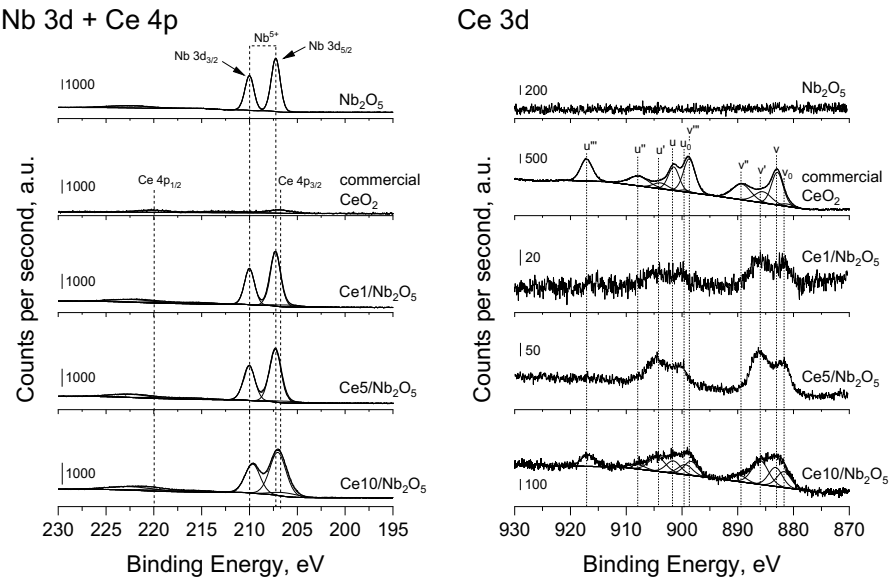

Fig. 9. Nb 3d + Ce 4p (left) and Ce 3d (right) XP spectra of different catalysts studied in this work.

More information about oxidation state of cerium species in ceria-doped samples was provided by detailed analysis of Ce 3d spectra of $Ce10/Nb_2O_5$, for which the signal was the most intense. As shown in **Fig. 9**, relative contribution of XP peaks characteristic of Ce^{3+} species was significantly more pronounced for $Ce10/Nb_2O_5$ than that observed for commercial CeO_2. Since FTIR measurements for both samples did not reveal any noticeable IR band typical of methanol molecules adsorbed on Ce^{3+} cations, we claimed that higher relative contribution of XP peaks characteristic of Ce^{3+} species established for $Ce10/Nb_2O_5$ resulted most probably from higher concentration of defect sites in the structure of this catalyst (i.e. Ce^{4+} ions surrounded by oxygen vacancies in which electrons are trapped). As it was documented by Baldim et al. [54], concentration of defect sites on the surface of CeO_2 nanoparticles often increases with decreasing particle size. Since ceria species in all catalysts prepared by wet impregnation were highly dispersed on niobia surface, we claim that high concentration of the above-mentioned defect sites in the structure of these materials is very likely. It is worth noting that our hypothesis is in agreement with results of UV-vis studies, in which significant shift of the absorption edge of $Ce10/Nb_2O_5$ towards lower energy values was observed (see **Fig. 8b**).

To verify whether the ceria doping has any impact on recombination of charge carriers in the composite materials we have performed photoluminescence measurements. According to literature, the photoluminescence emission is mainly originated from radiative recombination of photo-generated electrons and holes trapped in the band tails of semiconductors [55]. The higher the emission intensity, the higher the efficiency of charge carriers recombination [56]. Undoped niobium pentoxide exhibited three broad emission peaks with maximum intensity at ca. 380, 425 and 500 nm (**Fig. 10**).

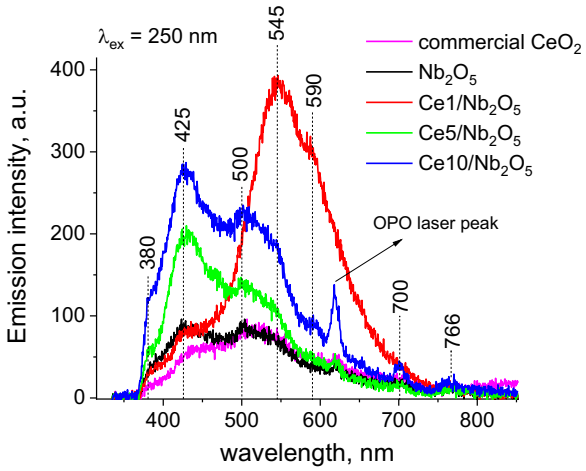

Fig. 10. Photoluminescence spectra of catalysts.

The emission peaks at ca. 380 and 425 nm exhibit energy close to the optical band gap of Nb_2O_5 (3.22 eV; see **Fig. 8b**) and may be attributed to near-band gap emission from Nb_2O_5 (recombination of photo-excited electrons in the Nb 4d conduction band and holes in the in the O 2p valance band of Nb_2O_5 [46]), while the green emission at ca. 500 nm may be related to the presence of structure defects, such as distorted NbO_6 octahedral groups [46,57] (charge transfer transitions form Nb^{5+} $4d^0$ state to O 2p orbital of oxygen ions in distorted NbO_6 octahedral [58]). In the case of commercial CeO_2, two main broad emission peaks at similar wavelengths as that observed for Nb_2O_5 can be identified (the first peak at ca. 425 nm and the second one at ca. 500 nm). The energy of the former emission peak (~2.92 eV) is close to the optical band gap of commercial CeO_2 (2.96 eV; see **Fig. 8b**). Thus, this emission peak can be attributed to the direct band to band recombination of charge carriers in CeO_2 (recombination of photo-excited electrons in the Ce 4f conduction band and holes in the O 2p valance band of CeO_2). According to literature [59,60], the latter broad emission peak can be attributed to the transitions from electronic energy levels of defects (mainly oxygen vacancies) localized below the Ce 4f band of the CeO_2 nanoparticles to the O 2p valence band of CeO_2. In the doped samples, loading of cerium species on niobia led to significant increase in emission intensity of composite materials at ca. 425, 500 and 545 nm (**Fig. 10**). Increased emission at ca. 425 nm may results both from

promoted recombination of photo-excited electrons in the Nb 4d conduction band and holes in the O 2p valence band of Nb_2O_5, and/or from promoted recombination of photo-generated charged carries in CeO_2. The emission energy of the peaks at ca. 500 nm (2.48 eV) and 545 nm (2.28 eV) is similar to the optical band gap of Ce10/Nb_2O_5 (optical band gap resulted from the presence of CeO_2 species with high concentration of defect sites; E_g ~ 2.52 eV; **Fig. 8b**). Thus, the increase in intensity of these emission peaks observed for ceria-doped samples may be attributed to improved charge recombination related to transitions from electronic energy levels of defects (mainly oxygen vacancies) localized below the Ce 4f band of the CeO_2 nanoparticles to the O 2p valence band of CeO_2.

3.3 Discussion on the role of ceria in deactivation of CeO_2/Nb_2O_5 heterostructures

Detailed characterization of as-prepared catalysts led us to observe that ceria species loaded on niobia surface by wet impregnation were not only highly dispersed but also strongly interacted with niobia support. As implied by UV-vis and XPS studies, such highly dispersed ceria species are substantially different from bulk CeO_2. The heterostructures prepared by wet impregnation exhibited much higher relative concentration of ceria lattice defects which were responsible for changes in electronic and optical properties of cerium species. As revealed by photoluminescence studies, defects sites in ceria lattice not only modified electronic and optical properties of cerium species but they acted also as recombination centers for photo-excited electrons and holes. To shed more light on recombination of the photo-induced charge carries in CeO_2/Nb_2O_5 heterostructures we have predicted theoretically the conduction (E_{CB}) and valence (E_{VB}) band edges of undoped Nb_2O_5 and commercial CeO_2 using the following empirical equations [20]:

$$E_{CB} = X - E^e - 0.5*E_g \qquad (1)$$

$$E_{VB} = E_g - E_{CB} \qquad (2)$$

where X is the absolute electronegativity of the semiconductor, obtained from the geometric mean of the electronegativity of its constituent atoms (X values for Nb_2O_5 and commercial CeO_2 are 5.55 eV [20] and 5.57 eV [48], respectively); E_g is the band gap of the semiconductor (3.22 eV and 2.96 eV for Nb_2O_5 and commercial CeO_2, respectively); E^e is the energy of free electrons *vs.* the hydrogen scale (4.5 eV). The calculated conduction band edge potential of Nb_2O_5 was found to be of -0.56 eV and is more negative than that of commercial CeO_2 (-0.41 eV). Corresponding valence band edge potential estimated for Nb_2O_5 was of 2.66 eV and more positive than that of commercial CeO_2 (2.55 eV). We propose that irradiation of mechanical mixture of the metal oxides with UV light resulted in formation of photo-excited electrons (e^-) and positively charged holes (h^+) both in CeO_2 and Nb_2O_5. According to the bands edge positions, the as-formed h^+ were transferred form valence band of Nb_2O_5 to valence band of commercial CeO_2. At the same time, photo-excited electrons from conduction band of Nb_2O_5 were transferred to conduction band of CeO_2. Thus, the band edge alignments in CeO_2/Nb_2O_5 heterostructures resulted in accumulation of both positively charged holes and photo-excited electrons in ceria species. We hypothesize that such accumulation of the charge carriers in ceria promotes their efficient recombination and diminishes the photocatalytic performance of mechanical mixtures of the metal oxides. More pronounced deactivation of the heterostructures prepared by wet impregnation resulted from two unique features of these materials. Firstly, ceria species in these materials were highly dispersed on niobia surface, providing great interface between the dopant and the support, and improving the photo-excited charge carriers transfer from one semiconductor to another. Secondly, such highly dispersed ceria species exhibited high concentration of defect sites which played the role of recombination centers for photo-generated electrons and holes, promoting their efficient recombination (see **Fig. 11**).

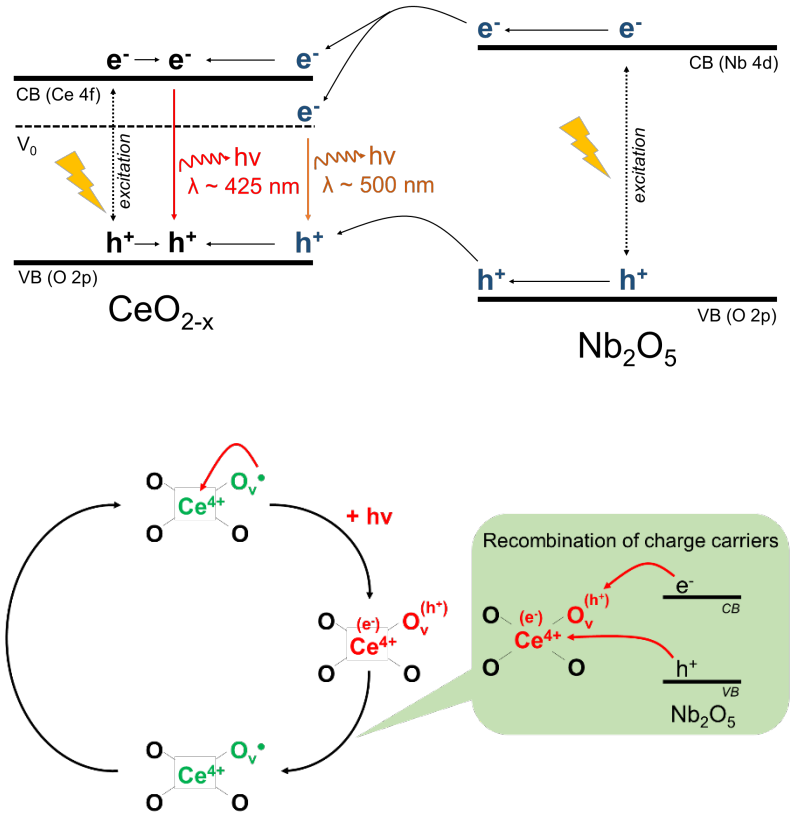

Fig. 11. Schematic representation of charge transfer process resulting in deactivation of ceria-doped Nb_2O_5 samples prepared by wet impregnation; CB – conduction band, VB – valence band, V_0 – energy level of defects (mainly oxygen vacancies – O_V) localized below the Ce 4f band of highly deficient ceria species (CeO_{2-x}) loaded on Nb_2O_5.

4 Conclusions

We demonstrated that addition of ceria dopant to niobium pentoxide led to significant decrease in photocatalytic activity of CeO_2/Nb_2O_5 nanostructures. We have established that at any given concentration of cerium species on niobia surface the photocatalytic activity of both CeO_2 and Nb_2O_5 in the composite material was totally quenched. *Operando*-IR studies demonstrated that deactivation of ceria-doped Nb_2O_5 samples resulted from quenching the catalysts ability to oxidize adsorbed methanol molecules. Deeper insight into the mechanism of photocatalytic process provided by photoluminescence measurements showed that deactivation

of heterostructures and ineffective oxidation originated from promoting the recombination of photo-generated charge carriers. The main factors responsible for efficient recombination of photo-excited electrons and holes in the composite catalysts were high dispersion of ceria species on niobia surface, which provided excessive interface between these two semiconductors, and high concentration of defect sites in the structure of such ultrafine ceria species (also shown by IR spectra of chemisorbed methanol) which acted as recombination centers for photo-excited charge carriers.

The results obtained in this study provide deep insight into the role of ceria dopant in controlling the photocatalytic activity of semiconductor-based photocatalyst. It is expected that this new fundamental knowledge about quenching of niobia activity by doping with ceria may play an important role in development of new composite nanomaterials as UV filters. Furthermore, the knowledge about the origin of poisoning effect of Nb_2O_5 by ceria species is important for developing future heterogeneous ceria-doped photocatalysts too. In case of the Nb_2O_5, a doping with ceria will require a linker promoting a Z-scheme charge transfer (electron or hole) from niobia to ceria and minimizing the ceria/niobia interfaces.

Acknowledgments

National Science Centre, Poland (Grant No. 2018/28/C/ST5/00255) is acknowledged for the financial support of this work. PXRD studies performed by C.P.H. and K.K. were supported by National Science Foundation DMR-2003783 grant. Lukasz Wolski wishes to thank prof. Marcin Ziolek and Maria Ziolek (Adam Mickiewicz University, Poznań, Poland) for very helpful discussions and Adrian Walkowiak (Adam Mickiewicz University, Poznań, Poland) for nitrogen physisorption measurements.

Appendix A. Supporting Information

FTIR spectra of catalyst surfaces at the beginning of methanol adsorption under dark conditions **(Fig. S1)**; Crystal structure of the derived Nb_2O_5 model (*Cmmm*) **(Fig. S2)**; PXRD patterns for Ce/Nb_2O_5 samples collected with Si (NIST Si 640d) internal standard **(Fig. S3)**; Bright field and HAADF-STEM low magnification images of Nb_2O_5 sample, and overview bright field HRTEM image and corresponding ED pattern indexed based on orthorhombic *Cmmm* structure **(Fig. S4)**.

Declaration of competing interest

The authors declare that they have no known competing financial interests or personal relationships that could have appeared to influence the work reported in this paper.

References

(1) Montini, T.; Melchionna, M.; Monai, M.; Fornasiero, P. Fundamentals and Catalytic Applications of CeO_2-Based Materials. *Chem. Rev.* **2016**, *116* (10), 5987–6041. https://doi.org/10.1021/acs.chemrev.5b00603.

(2) Bakkiyaraj, R.; Bharath, G.; Hasini Ramsait, K.; Abdel-Wahab, A.; Alsharaeh, E. H.; Chen, S. M.; Balakrishnan, M. Solution Combustion Synthesis and Physico-Chemical Properties of Ultrafine CeO_2 Nanoparticles and Their Photocatalytic Activity. *RSC Adv.* **2016**, *6* (56), 51238–51245. https://doi.org/10.1039/c6ra00382f.

(3) Cui, Z.; Zhou, H.; Wang, G.; Zhang, Y.; Zhang, H.; Zhao, H. Enhancement of the Visible-Light Photocatalytic Activity of CeO_2 by Chemisorbed Oxygen in the Selective Oxidation of Benzyl Alcohol. *New J. Chem.* **2019**, *43* (19), 7355–7362. https://doi.org/10.1039/c9nj01098j.

(4) Majumder, D.; Chakraborty, I.; Mandal, K.; Roy, S. Facet-Dependent Photodegradation

of Methylene Blue Using Pristine CeO_2 Nanostructures. *ACS Omega* **2019**, *4* (2), 4243–4251. https://doi.org/10.1021/acsomega.8b03298.

(5) Hamoud, I. H.; Finqueneisel, G.; Azambre, B. Removal of Binary Dyes Mixtures with Opposite and Similar Charges by Adsorption, Coagulation/Flocculation and Catalytic Oxidation in the Presence of CeO_2/H_2O_2 Fenton-like System. *J. Environ. Manage.* **2017**, *195*, 195–207. https://doi.org/10.1016/j.jenvman.2016.07.067.

(6) Cai, W.; Chen, F.; Shen, X.; Chen, L.; Zhang, J. Enhanced Catalytic Degradation of AO7 in the CeO_2-H_2O_2 system with Fe^{3+} doping. *Appl. Catal. B Environ.* **2010**, *101* (1–2), 160–168. https://doi.org/10.1016/j.apcatb.2010.09.031.

(7) Chen, F.; Shen, X.; Wang, Y.; Zhang, J. CeO_2/H_2O_2 system Catalytic Oxidation Mechanism Study via a Kinetics Investigation to the Degradation of Acid Orange 7. *Appl. Catal. B Environ.* **2012**, *121–122*, 223–229. https://doi.org/10.1016/j.apcatb.2012.04.014.

(8) Zhu, L.; Li, H.; Xia, P.; Liu, Z.; Xiong, D. Hierarchical ZnO Decorated with CeO_2 Nanoparticles as the Direct Z-Scheme Heterojunction for Enhanced Photocatalytic Activity. *ACS Appl. Mater. Interfaces* **2018**, *10* (46), 39679–39687. https://doi.org/10.1021/acsami.8b13782.

(9) Muñoz-Batista, M. J.; Gómez-Cerezo, M. N.; Kubacka, A.; Tudela, D.; Fernández-García, M. Role of Interface Contact in CeO_2-TiO_2 Photocatalytic Composite Materials. *ACS Catal.* **2014**, *4* (1), 63–72. https://doi.org/10.1021/cs400878b.

(10) Eskandarloo, H.; Badiei, A.; Behnajady, M. A. TiO_2/CeO_2 Hybrid Photocatalyst with Enhanced Photocatalytic Activity: Optimization of Synthesis Variables. *Ind. Eng. Chem. Res.* **2014**, *53* (19), 7847–7855. https://doi.org/10.1021/ie403460d.

(11) Morlando, A.; Chaki Borrás, M.; Rehman, Y.; Bakand, S.; Barker, P.; Sluyter, R.; Konstantinov, K. Development of CeO_2 Nanodot Encrusted TiO_2 Nanoparticles with Reduced Photocatalytic Activity and Increased Biocompatibility towards a Human Keratinocyte Cell Line. *J. Mater. Chem. B* **2020**, *8* (18), 4016–4028. https://doi.org/10.1039/d0tb00629g.

(12) Mueen, R.; Morlando, A.; Qutaish, H.; Lerch, M.; Cheng, Z.; Konstantinov, K. ZnO/CeO_2 Nanocomposite with Low Photocatalytic Activity as Efficient UV Filters. *J. Mater. Sci.* **2020**, *55* (16), 6834–6847. https://doi.org/10.1007/s10853-020-04493-x.

(13) Su, K.; Liu, H.; Gao, Z.; Fornasiero, P.; Wang, F. Nb_2O_5 -Based Photocatalysts. *Adv. Sci.* **2021**, 2003156. https://doi.org/10.1002/advs.202003156.

(14) Riente, P.; Noël, T. Application of Metal Oxide Semiconductors in Light-Driven Organic Transformations. *Catal. Sci. Technol.* **2019**, *9* (19), 5186–5232. https://doi.org/10.1039/c9cy01170f.

(15) Tamai, K.; Hosokawa, S.; Teramura, K.; Shishido, T.; Tanaka, T. Synthesis of Niobium Oxide Nanoparticles with Plate Morphology Utilizing Solvothermal Reaction and Their Performances for Selective Photooxidation. *Appl. Catal. B Environ.* **2016**, *182*, 469–475. https://doi.org/10.1016/j.apcatb.2015.10.003.

(16) Kulkarni, A. K.; Praveen, C. S.; Sethi, Y. A.; Panmand, R. P.; Arbuj, S. S.; Naik, S. D.; Ghule, A. V.; Kale, B. B. Nanostructured N-Doped Orthorhombic Nb_2O_5 as an Efficient Stable Photocatalyst for Hydrogen Generation under Visible Light. *Dalt. Trans.* **2017**, *46* (43), 14859–14868. https://doi.org/10.1039/c7dt02611k.

(17) Zhao, Y.; Eley, C.; Hu, J.; Foord, J. S.; Ye, L.; He, H.; Tsang, S. C. E. Shape-Dependent Acidity and Photocatalytic Activity of Nb_2O_5 Nanocrystals with an Active TT (001) Surface. *Angew. Chemie - Int. Ed.* **2012**, *51* (16), 3846–3849.

https://doi.org/10.1002/anie.201108580.

(18) Nowak, I.; Ziolek, M. Niobium Compounds: Preparation, Characterization, and Application in Heterogeneous Catalysis. *Chem. Rev.* **1999**, *99*, 3603–3624.

(19) Ftouni, K.; Lakiss, L.; Thomas, S.; Daturi, M.; Fernandez, C.; Bazin, P.; El Fallah, J.; El-Roz, M. TiO_2/Zeolite Bifunctional (Photo)Catalysts for a Selective Conversion of Methanol to Dimethoxymethane: On the Role of Brønsted Acidity. *J. Phys. Chem. C* **2018**, *122* (51), 29359–29367. https://doi.org/10.1021/acs.jpcc.8b10092.

(20) Yan, J.; Wu, G.; Guan, N.; Li, L. Nb_2O_5/TiO_2 Heterojunctions: Synthesis Strategy and Photocatalytic Activity. *Appl. Catal. B Environ.* **2014**, *152–153* (1), 280–288. https://doi.org/10.1016/j.apcatb.2014.01.049.

(21) De Andrade, F. V.; De Lima, G. M.; Augusti, R.; Coelho, M. G.; Assis, Y. P. Q.; Machado, I. R. M. A New Material Consisting of TiO_2 Supported on Nb_2O_5 as Photocatalyst for the Degradation of Organic Contaminants in Aqueous Medium. *J. Environ. Chem. Eng.* **2014**, *2* (4), 2352–2358. https://doi.org/10.1016/j.jece.2014.02.004.

(22) Lam, S. M.; Sin, J. C.; Satoshi, I.; Abdullah, A. Z.; Mohamed, A. R. Enhanced Sunlight Photocatalytic Performance over Nb_2O_5/ZnO Nanorod Composites and the Mechanism Study. *Appl. Catal. A Gen.* **2014**, *471*, 126–135. https://doi.org/10.1016/j.apcata.2013.12.001.

(23) Wu, J.; Li, J.; Liu, J.; Bai, J.; Yang, L. A Novel Nb_2O_5/Bi_2WO_6 Heterojunction Photocatalytic Oxidative Desulfurization Catalyst with High Visible Light-Induced Photocatalytic Activity. *RSC Adv.* **2017**, *7* (81), 51046–51054. https://doi.org/10.1039/c7ra09829d.

(24) Hashemzadeh, F.; Gaffarinejad, A.; Rahimi, R. Porous p-NiO/n-Nb_2O_5 Nanocomposites Prepared by an EISA Route with Enhanced Photocatalytic Activity in Simultaneous Cr(VI) Reduction and Methyl Orange Decolorization under Visible Light Irradiation. *J. Hazard. Mater.* **2015**, *286*, 64–74. https://doi.org/10.1016/j.jhazmat.2014.12.038.

(25) Hong, Y.; Li, C.; Zhang, G.; Meng, Y.; Yin, B.; Zhao, Y.; Shi, W. Efficient and Stable Nb_2O_5 Modified g-C_3N_4 Photocatalyst for Removal of Antibiotic Pollutant. *Chem. Eng. J.* **2016**, *299*, 74–84. https://doi.org/10.1016/j.cej.2016.04.092.

(26) Tatibouet, J. M. Methanol Oxidation as a Catalytic Surface Probe. *Appl. Catal. A Gen.* **1977**, *148*, 213–252. https://doi.org/10.1016/S0926-860X(96)00236-0.

(27) Kähler, K.; Holz, M. C.; Rohe, M.; Van Veen, A. C.; Muhler, M. Methanol Oxidation as Probe Reaction for Active Sites in Au/ZnO and Au/TiO_2 Catalysts. *J. Catal.* **2013**, *299*, 162–170. https://doi.org/10.1016/j.jcat.2012.12.001.

(28) Crampton, A. S.; Cai, L.; Janvelyan, N.; Zheng, X.; Friend, C. M. Methanol Photo-Oxidation on Rutile TiO_2 Nanowires: Probing Reaction Pathways on Complex Materials. *J. Phys. Chem. C* **2017**, *121* (18), 9910–9919. https://doi.org/10.1021/acs.jpcc.7b01385.

(29) Murayama, T.; Chen, J.; Hirata, J.; Matsumoto, K.; Ueda, W. Hydrothermal Synthesis of Octahedra-Based Layered Niobium Oxide and Its Catalytic Activity as a Solid Acid. *Catal. Sci. Technol.* **2014**, *4* (12), 4250–4257. https://doi.org/10.1039/C4CY00713A.

(30) Toby, B. H.; Von Dreele, R. B. GSAS-II: The Genesis of a Modern Open-Source All Purpose Crystallography Software Package. *J. Appl. Crystallogr.* **2013**, *46* (2), 544–549. https://doi.org/10.1107/S0021889813003531.

(31) Wuttke, S.; Bazin, P.; Vimont, A.; Serre, C.; Seo, Y. K.; Hwang, Y. K.; Chang, J. S.; Férey, G.; Daturi, M. Discovering the Active Sites for C3 Separation in MIL-100(Fe) by

Using Operando IR Spectroscopy. *Chem. - A Eur. J.* **2012**, *18* (38), 11959–11967. https://doi.org/10.1002/chem.201201006.

(32) El-Roz, M.; Bazin, P.; Thibault-Starzyk, F. An Operando-IR Study of Photocatalytic Reaction of Methanol on New *BEA Supported TiO_2 Catalyst. *Catal. Today* **2013**, *205*, 111–119. https://doi.org/10.1016/j.cattod.2012.08.023.

(33) El-Roz, M.; Kus, M.; Cool, P.; Thibault-Starzyk, F. New Operando IR Technique to Study the Photocatalytic Activity and Selectivity of TiO_2 nanotubes in Air Purification: Influence of Temperature, UV Intensity, and VOC Concentration. *J. Phys. Chem. C* **2012**, *116* (24), 13252–13263. https://doi.org/10.1021/jp3034819.

(34) El-Roz, M.; Bazin, P.; Daturi, M.; Thibault-Starzyk, F. On the Mechanism of Methanol Photooxidation to Methylformate and Carbon Dioxide on TiO_2: An Operando-FTIR Study. *Phys. Chem. Chem. Phys.* **2015**, *17* (17), 11277–11283. https://doi.org/10.1039/C5CP00726G.

(35) Binet, C.; Daturi, M.; Lavalley, J.-C. IR Study of Polycrystalline Ceria Properties in Oxidised and Reduced States. *Catal. Today* **1999**, *50* (2), 207–225. https://doi.org/10.1016/S0920-5861(98)00504-5.

(36) Daturi, M.; Finocchio, E.; Binet, C.; Lavalley, J. C.; Fally, F.; Perrichon, V. Study of Bulk and Surface Reduction by Hydrogen of $Ce_xZr_{1-x}O_2$ Mixed Oxides Followed by FTIR Spectroscopy and Magnetic Balance. *J. Phys. Chem. B* **1999**, *103* (23), 4884–4891. https://doi.org/10.1021/jp9905981.

(37) Kähler, K.; Holz, M. C.; Rohe, M.; Strunk, J.; Muhler, M. Probing the Reactivity of ZnO and Au/ZnO Nanoparticles by Methanol Adsorption: A TPD and DRIFTS Study. *ChemPhysChem* **2010**, *11* (12), 2521–2529. https://doi.org/10.1002/cphc.201000282.

(38) Daturi, M.; Binet, C.; Lavalley, J.-C.; Galtayries, A.; Sporken, R. Surface Investigation on $Ce_xZr_{1-x}O_2$ Compounds. *Phys. Chem. Chem. Phys.* **1999**, *1* (24), 5717–5724. https://doi.org/10.1039/a905758g.

(39) Kaichev, V. V.; Popova, G. Y.; Chesalov, Y. A.; Saraev, A. A.; Zemlyanov, D. Y.; Beloshapkin, S. A.; Knop-Gericke, A.; Schlögl, R.; Andrushkevich, T. V.; Bukhtiyarov, V. I. Selective Oxidation of Methanol to Form Dimethoxymethane and Methyl Formate over a Monolayer V_2O_5/TiO_2 Catalyst. *J. Catal.* **2014**, *311*, 59–70. https://doi.org/10.1016/j.jcat.2013.10.026.

(40) Moulin, B.; Oliviero, L.; Bazin, P.; Daturi, M.; Costentin, G.; Maugé, F. How to Determine IR Molar Absorption Coefficients of Co-Adsorbed Species? Application to Methanol Adsorption for Quantification of MgO Basic Sites. *Phys. Chem. Chem. Phys.* **2011**, *13* (22), 10797–10807. https://doi.org/10.1039/c0cp02767g.

(41) Schmid, S.; Fung, V. Incommensurate Modulated Structures in the Ta_2O_5-Al_2O_3 System. *Aust. J. Chem.* **2012**, *65* (7), 851–859. https://doi.org/10.1071/CH12080.

(42) Thommes, M.; Kaneko, K.; Neimark, A. V.; Olivier, J. P.; Rodriguez-Reinoso, F.; Rouquerol, J.; Sing, K. S. W. Physisorption of Gases, with Special Reference to the Evaluation of Surface Area and Pore Size Distribution (IUPAC Technical Report). *Pure Appl. Chem.* **2015**, *87* (9–10), 1051–1069. https://doi.org/10.1515/pac-2014-1117.

(43) Armaroli, T.; Busca, G.; Carlini, C.; Giuttari, M.; Raspolli Galletti, A. M.; Sbrana, G. Acid Sites Characterization of Niobium Phosphate Catalysts and Their Activity in Fructose Dehydration to 5-Hydroxymethyl-2-Furaldehyde. *J. Mol. Catal. A Chem.* **2000**, *151* (1–2), 233–243. https://doi.org/10.1016/S1381-1169(99)00248-4.

(44) Liu, L.; Yao, Z.; Liu, B.; Dong, L. Correlation of Structural Characteristics with Catalytic Performance of $CuO/Ce_xZr_{1-x}O_2$ catalysts for NO Reduction by CO. *J. Catal.* **2010**, *275*

(1), 45–60. https://doi.org/10.1016/j.jcat.2010.07.024.

(45) Reddy, B. M.; Bharali, P.; Saikia, P.; Park, S. E.; Van Den Berg, M. W. E.; Muhler, M.; Grünert, W. Structural Characterization and Catalytic Activity of Nanosized $Ce_xM_{1-x}O_2$ (M = Zr and Hf) Mixed Oxides. *J. Phys. Chem. C* **2008**, *112* (31), 11729–11737. https://doi.org/10.1021/jp802674m.

(46) Zhou, Y.; Qiu, Z.; Lü, M.; Zhang, A.; Ma, Q. Preparation and Spectroscopic Properties of Nb_2O_5 Nanorods. *J. Lumin.* **2008**, *128* (8), 1369–1372. https://doi.org/10.1016/j.jlumin.2008.01.001.

(47) Channei, D.; Inceesungvorn, B.; Wetchakun, N.; Ukritnukun, S.; Nattestad, A.; Chen, J.; Phanichphant, S. Photocatalytic Degradation of Methyl Orange by CeO_2 and Fe–doped CeO_2 Films under Visible Light Irradiation. *Sci. Rep.* **2015**, *4* (1), 5757. https://doi.org/10.1038/srep05757.

(48) Arul, N. S.; Mangalaraj, D.; Ramachandran, R.; Grace, A. N.; Han, J. I. Fabrication of CeO_2/Fe_2O_3 Composite Nanospindles for Enhanced Visible Light Driven Photocatalysts and Supercapacitor Electrodes. *J. Mater. Chem. A* **2015**, *3* (29), 15248–15258. https://doi.org/10.1039/c5ta02630j.

(49) Ansari, S. A.; Khan, M. M.; Ansari, M. O.; Kalathil, S.; Lee, J.; Cho, M. H. Band Gap Engineering of CeO_2 Nanostructure Using an Electrochemically Active Biofilm for Visible Light Applications. *RSC Adv.* **2014**, *4* (32), 16782–16791. https://doi.org/10.1039/c4ra00861h.

(50) Liu, H.; Gao, N.; Liao, M.; Fang, X. Hexagonal-like Nb_2O_5 Nanoplates-Based Photodetectors and Photocatalyst with High Performances. *Sci. Rep.* **2015**, *5* (1), 7716. https://doi.org/10.1038/srep07716.

(51) Bêche, E.; Charvin, P.; Perarnau, D.; Abanades, S.; Flamant, G. Ce 3d XPS Investigation of Cerium Oxides and Mixed Cerium Oxide ($Ce_xTi_yO_z$). *Surf. Interface Anal.* **2008**, *40* (3–4), 264–267. https://doi.org/10.1002/sia.2686.

(52) Pereira-Hernández, X. I.; DeLaRiva, A.; Muravev, V.; Kunwar, D.; Xiong, H.; Sudduth, B.; Engelhard, M.; Kovarik, L.; Hensen, E. J. M.; Wang, Y.; Datye, A. K. Tuning Pt-CeO_2 Interactions by High-Temperature Vapor-Phase Synthesis for Improved Reducibility of Lattice Oxygen. *Nat. Commun.* **2019**, *10* (1), 1358. https://doi.org/10.1038/s41467-019-09308-5.

(53) Lei, W.; Zhang, T.; Gu, L.; Liu, P.; Rodriguez, J. A.; Liu, G.; Liu, M. Surface-Structure Sensitivity of CeO_2 Nanocrystals in Photocatalysis and Enhancing the Reactivity with Nanogold. *ACS Catal.* **2015**, *5* (7), 4385–4393. https://doi.org/10.1021/acscatal.5b00620.

(54) Baldim, V.; Bedioui, F.; Mignet, N.; Margaill, I.; Berret, J. F. The Enzyme-like Catalytic Activity of Cerium Oxide Nanoparticles and Its Dependency on Ce^{3+} Surface Area Concentration. *Nanoscale* **2018**, *10* (15), 6971–6980. https://doi.org/10.1039/c8nr00325d.

(55) Georgiev, R.; Georgieva, B.; Vasileva, M.; Ivanov, P.; Babeva, T. Optical Properties of Sol-Gel Nb_2O_5 Films with Tunable Porosity for Sensing Applications. *Adv. Condens. Matter Phys.* **2015**, *2015*, 1–8. https://doi.org/10.1155/2015/403196.

(56) Khan, M. E.; Khan, M. M.; Cho, M. H. Ce^{3+}-Ion, Surface Oxygen Vacancy, and Visible Light-Induced Photocatalytic Dye Degradation and Photocapacitive Performance of CeO_2-Graphene Nanostructures. *Sci. Rep.* **2017**, *7* (1), 5928. https://doi.org/10.1038/s41598-017-06139-6.

(57) Chen, Q. Nb_2O_5 Improved Photoluminescence, Magnetic and Faraday Rotation

Properties of Magneto-Optical Glasses. *J. Non. Cryst. Solids* **2019**, *519*, 119451. https://doi.org/10.1016/j.jnoncrysol.2019.05.027.

(58) Zeng, H.; Song, J.; Chen, D.; Yuan, S.; Jiang, X.; Cheng, Y.; Yang, Y.; Chen, G. Three-Photon-Excited Upconversion Luminescence of Niobium Ions Doped Silicate Glass by a Femtosecond Laser Irradiation. *Opt. Express* **2008**, *16* (9), 6502. https://doi.org/10.1364/oe.16.006502.

(59) Kumar, S.; Ojha, A. K.; Patrice, D.; Yadav, B. S.; Materny, A. One-Step in Situ Synthesis of CeO_2 Nanoparticles Grown on Reduced Graphene Oxide as an Excellent Fluorescent and Photocatalyst Material under Sunlight Irradiation. *Phys. Chem. Chem. Phys.* **2016**, *18* (16), 11157–11167. https://doi.org/10.1039/c5cp04457j.

(60) Hemalatha, K. S.; Rukmani, K. Synthesis, Characterization and Optical Properties of Polyvinyl Alcohol-Cerium Oxide Nanocomposite Films. *RSC Adv.* **2016**, *6* (78), 74354–74366. https://doi.org/10.1039/c6ra11126b.